ACS APPLIED MATERIALS & INTERFACES

Research Article

www.acsami.org

Effect of Ni^{2+} Content on Lithium/Nickel Disorder for Ni-Rich Cathode Materials

Feng Wu,[†,‡] Jun Tian,[†] Yuefeng Su,*[,†,‡] Jing Wang,[†,‡] Cunzhong Zhang,[†,‡] Liying Bao,[†,‡] Tao He,[†] Jinghui Li,[†] and Shi Chen[†,‡]

[†]Beijing Key Laboratory of Environmental Science and Engineering, School of Chemical Engineering and Environment, Beijing Institute of Technology, Beijing 100081, China

[‡]National Development Center of High Technology Green Materials, Beijing 100081, China

Supporting Information

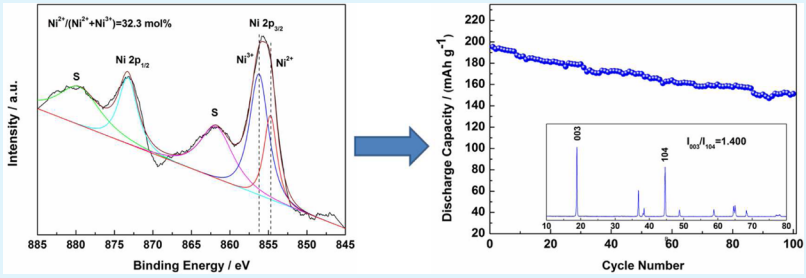

ABSTRACT: Li excess $LiNi_{0.8}Co_{0.1}Mn_{0.1}O_2$ was produced by sintering the $Ni_{0.8}Co_{0.1}Mn_{0.1}(OH)_2$ precursor with different amounts of a lithium source. X-ray photoelectron spectroscopy confirmed that a greater excess of Li^+ leads to an increase in the number of Ni^{2+} ions. Interestingly, the level of Li^+/Ni^{2+} disordering decreases with an increase in Ni^{2+} content determined by the I_{003}/I_{104} ratio in the X-ray diffraction patterns. The electrochemical measurement shows that the cycling stability and rate capability improve with an increase in Ni^{2+} content. After cycling, electrochemical impedance spectroscopy shows decreased charge transfer resistance, and the XRD patterns exhibit an increased I_{003}/I_{104} ratio with an increase in Ni^{2+} content, reflecting the decrease in the level of Li^+/Ni^{2+} disorder during cycling.

KEYWORDS: *lithium-ion batteries, cathode material, nickel-rich, cation disorder, electrochemical properties*

1. INTRODUCTION

Rechargeable lithium-ion batteries (LIBs) with high energy and high power density are critically needed for applications in electric vehicles (EVs) and large-scale energy storage.[1−4] The lack of good electrochemical performance for cathode materials is a technological bottleneck for obtaining advanced LIBs.[5] Among the cathode materials, layered Ni-rich $LiNi_{1-x}M_xO_2$ (M = Co or Mn; $1 - x > 0.5$) oxides have been intensively studied because of their high capacity (>200 mAh g^{-1}) above a charge of 4.5 V, relatively low cost, and environmental benignancy. However, these materials suffer from a poor cycle life and thermal stability,[6−11] which have impeded its commercialization. The impact of a Li^+/Ni^{2+} cation disordered distribution is one of the main reasons to induce the decrease in irreversible capacity.[12−14]

Much effort has been devoted to improving the electrochemical performance and structural stability of Ni-rich cathode materials. Among them, surface (MoO_3, Al_2O_3, CeO_2, etc.) coating[15−17] was shown to be an effective method. Designing a heterostructural shell surrounding the layered Ni-rich core was also intensively reported to increase the structural stability.[7−9,18−20] All the work mentioned above could protect the Ni-rich materials to reduce the level of Li^+/Ni^{2+} mixing during cycling.

In this work, $LiNi_{0.8}Co_{0.1}Mn_{0.1}O_2$ was selected as a typical cathode material for study. The nickel ions in Ni-rich oxides usually have two valence states (+2 and +3). The $Ni^{2+}/(Ni^{2+} + Ni^{3+})$ ratio is controlled by adding different amounts of the Li source, and the effect of Ni^{2+} content on the Li^+/Ni^{2+} disordered distribution with the corresponding electrochemical performance is discussed.

2. EXPERIMENTAL SECTION

2.1. Synthesis and Characterization. The precursor was synthesized by a coprecipitation method. An aqueous solution of $MnSO_4$, $NiSO_4$, and $CoSO_4$ with a concentration of 1 mol L^{-1} was pumped into a continuous stirred tank reactor under an Ar atmosphere. At the same time, a 1 mol L^{-1} NaOH solution with a desired amount of $NH_3{\cdot}H_2O$ was also pumped into the tank reactor. The stirring speed of 1000 rpm was maintained during the process, and the pH was kept at a constant value of 11 by adding $NH_3{\cdot}H_2O$. After the reaction, the precipitates were isolated by vacuum filtration, washed multiple times with distilled deionized water, and dried in a vacuum oven. The dried precipitations were mixed with a required amount of $LiOH{\cdot}H_2O$, preliminarily fired at 450 °C for 6 h, and then

Received: January 21, 2015
Accepted: March 26, 2015
Published: March 26, 2015

DOI: 10.1021/acsami.5b00645
ACS Appl. Mater. Interfaces 2015, 7, 7702−7708

calcined at 800 °C for 12 h in air. The final products with Li excesses of 0, 10, 20, and 30% were named E0–E3, respectively.

The crystal structure of all the as-prepared and cycled materials was measured by X-ray powder diffraction (XRD) (Rigaku UltimaIV-185) with Cu Kα radiation at a scan rate of 4° 2θ/min. The morphology of the particles was determined by field emission scanning electron microscopy (FESEM, FEI QUANTA 250). The chemical compositions of the samples were analyzed by inductively coupled plasma atomic emission spectrometry (ICP-AES). The valence states of Ni, Co, and Mn ions were examined by X-ray photoelectron spectroscopy (XPS). During XPS measurements, the base pressure of the sample chamber was kept below 3.0×10^{-10} mbar.

2.2. Electrochemical Measurement. The working electrodes were prepared by a slurry coating procedure. The slurry consisted of 80 wt % as-prepared materials, 10 wt % carbon conductive agents (carbon black), and 10 wt % polyvinylidene fluoride (PVDF) in an *N*-methyl pyrrolidone (NMP) solvent coated onto aluminum foil. The coated aluminum foil was dried at 100 °C for 36 h and punched into 15 mm diameter discs. Then the electrodes were assembled into CR2025 coin-type cells with Li electrodes and the electrolyte [1 M $LiPF_6$ in a 1/1/1 (v/v) EC/EMC/DMC mixture] in an Ar-filled glovebox. The cells were cycled galvanostatically between 2.7 and 4.6 V (vs Li^+/Li) at desired current densities at room temperature using a CT2001A Land instrument. The electrochemical impedance spectroscopy (EIS) measurements were conducted with a CHI660A impedance analyzer, using a frequency range of 100 kHz to 0.01 Hz.

3. RESULTS AND DISCUSSION

The XRD patterns and the morphologies of the precursor are shown in Figure 1. The XRD patterns (Figure 1a) confirm that

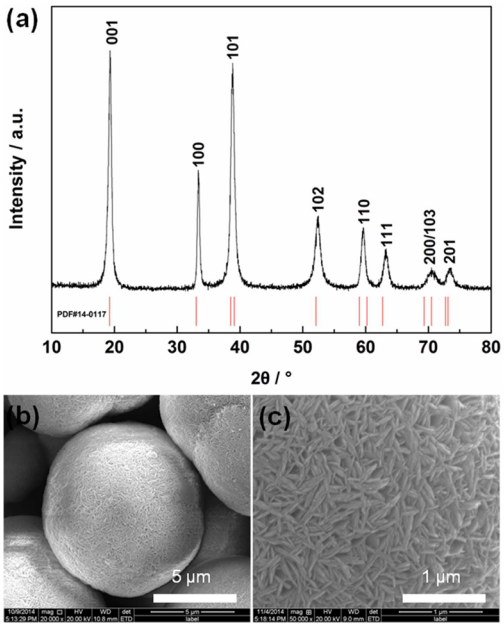

Figure 1. (a) XRD patterns and (b and c) SEM images of the precursor.

the precursor is typical $Ni_{0.8}Co_{0.1}Mn_{0.1}(OH)_2$.[18,20] The precursor particles are microspheres with a diameter of ~8 μm (Figure 1b) and are composed of striplike primary particles (Figure 1c).

The XRD patterns of samples E0–E2 are shown in Figure 2. All the patterns are well-indexed with a layered hexagonal α-$NaFeO_2$ structure belonging to space group $R\bar{3}m$. The clear splitting of (006)/(102) and (018)/(110) peaks demonstrates the high degree of layered structure crystallization[21,22] for all

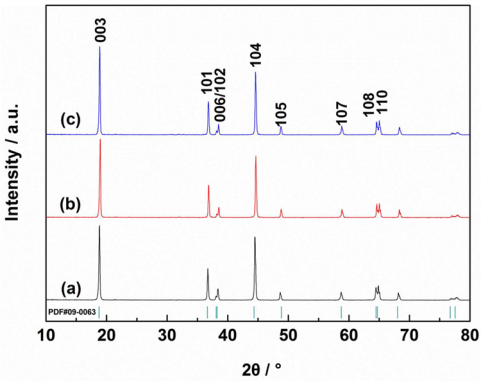

Figure 2. XRD patterns of samples (a) E0, (b) E1, and (c) E2.

the samples. XRD data analyses showed that the I_{003}/I_{104} intensity ratios for E0–E2 were 1.175, 1.271, and 1.400 (Table 1), respectively, indicating that E2 has the least Li^+/Ni^{2+}

Table 1. XRD Parameters of Samples E0–E2

sample	a (Å)	c (Å)	c/a (Å)	I_{003}/I_{104}
E0	2.87237	14.19354	4.9414	1.175
E1	2.86728	14.17037	4.9421	1.271
E2	2.86690	14.17463	4.9442	1.400

disorder.[22] The XRD patterns of sample E3 are shown in Figure S1b of the Supporting Information, and the main patterns are consistent with the layered structure. The I_{003}/I_{104} ratio for E3 is 1.139, showing that the Li^+/Ni^{2+} disorder is more serious compared with the disorder of other samples. Some minor peaks assigned to LiOH and Li_2CO_3 emerged because some amount of LiOH remains and reacts with CO_2 in air to form Li_2CO_3 during the synthetic process. The Li_2CO_3/LiOH impurity is electrochemically inactive with respect to lithium intercalation/deintercalation and responsible for the loss of capacity of the cathode material.[23,24] For this reason, we assume E3 has poor electrochemical properties, which is certified in the following electrochemical measurement.

Morphologies of E0, E1, and E2 characterized by SEM are shown in Figure 3 (E3 in Figure S1a of the Supporting Information). We observed that all the samples have a microspherical morphology with a diameter of ~8 μm. However, the primary particles composing the spheres are growing larger averagely with an increasing amount of the Li source, and the spheres are becoming less compact. The LiOH/Li_2CO_3 impurities that existed in sample E3 are thought to be too thin that they cannot be observed in the SEM image.

The measured XPS spectra of Ni 2p for samples E0–E2 are shown in Figure 4 (Mn 2p and Co 2p in Figure S2 of the Supporting Information). The most intense Ni $2p_{3/2}$ peak shifted from a higher binding energy of 856.7 eV to a lower binding energy of 855.8 eV with an increasing amount of the lithium source, suggesting that the amount of Ni^{2+} in samples E0–E2 is progressively increased. The fitting results show that the relative contents of Ni^{2+} are 27.1, 29.4, and 32.3 mol % for samples E0–E2, respectively, because more Ni^{3+} is reduced to Ni^{2+} with an increasing amount of submitted Li^+ to maintain the balance of valence states.

During the synthesis process by which $LiOH \cdot H_2O$ decomposes into LiOH and H_2O(g), some amount of Li will inevitably be lost because of the evaporation of a minor amount

DOI: 10.1021/acsami.5b00645
ACS Appl. Mater. Interfaces 2015, 7, 7702–7708

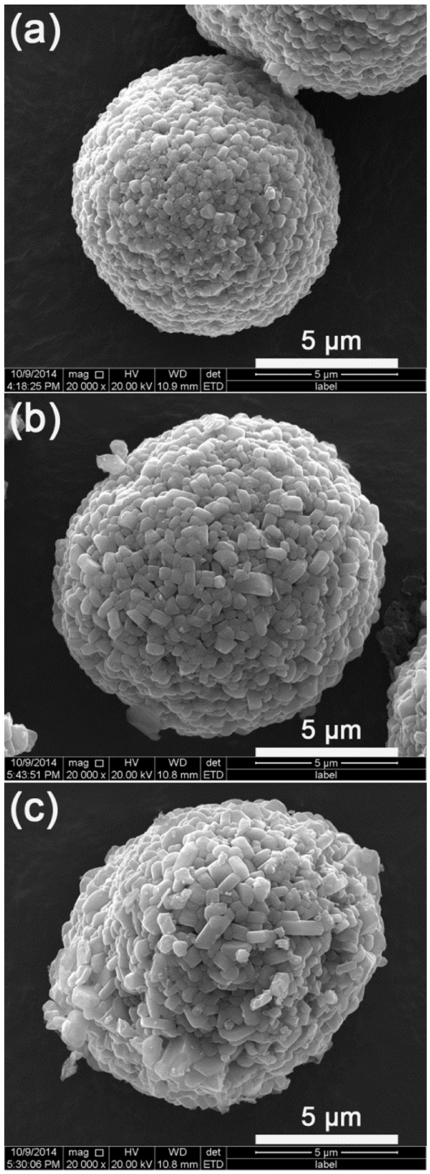

Figure 3. SEM images of samples (a) E0, (b) E1, and (c) E2.

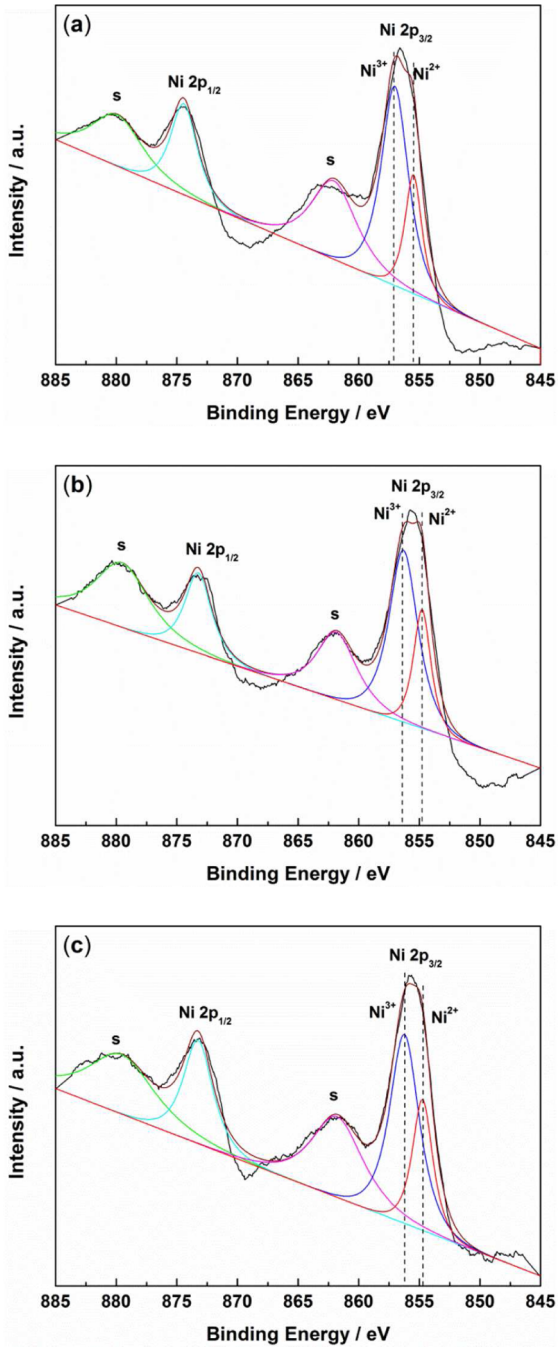

Figure 4. XPS spectra of Ni 2p for samples (a) E0, (b) E1, and (c) E2.

Table 2. Li/Ni/Co/Mn Molar Ratios from ICP-AES for Samples E0−E2

sample	Li/Ni/Co/Mn molar ratio
E0	0.994/0.794/0.108/0.102
E1	1.021/0.776/0.105/0.098
E2	1.051/0.755/0.101/0.093

of LiOH. The real chemical compositions of the samples were analyzed by ICP-AES. From the testing results shown in Table 2, we can conclude that the chemical compositions of samples E0−E2 are close to $Li_{0.994}Ni_{0.794}Co_{0.108}Mn_{0.102}O_2$, $Li_{1.021}Ni_{0.776}Co_{0.105}Mn_{0.098}O_2$, and $Li_{1.051}Ni_{0.755}Co_{0.101}Mn_{0.093}O_2$, respectively, because for Li^+/Ni^{2+} disordering, some Ni^{2+} ions are located in the Li layer and some Li^+ ions occupy the Ni^{2+} position in the transition metal layer. However, it is certain that the general atomic ratio of the number of atoms in the Li layer to the number of atoms in the transition metal layer [(Li + Ni)/(Li + Ni + Co + Mn)] equals 1.

The cycling performance and charge/discharge profiles of samples E0−E2 at 0.2 C (1 C = 200 mAh g^{-1}) between 2.7 and 4.6 V at room temperature are shown in Figure 5, and the corresponding electrochemical data are listed in Table 3. The initial and 100th discharge capacities of sample E0 are 217.4 and 120.6 mAh g^{-1}, respectively, with a capacity retention of only 55.5%, and it has an initial Coulombic efficiency of 81.2%. For sample E1, the initial discharge capacity (208.1 mAh g^{-1}) and the initial Coulombic efficiency (77.8%) decreased compared with those of E0. However, it has a more stable cycling performance with a capacity retention of 60.1% (125.0 mAh g^{-1}) after 100 cycles. For the E2 sample, the initial discharge capacity and initial Coulombic efficiency are further decreased; however, the cycling performance is further improved, and the discharge capacity is greatly enhanced to

DOI: 10.1021/acsami.5b00645
ACS Appl. Mater. Interfaces 2015, 7, 7702−7708

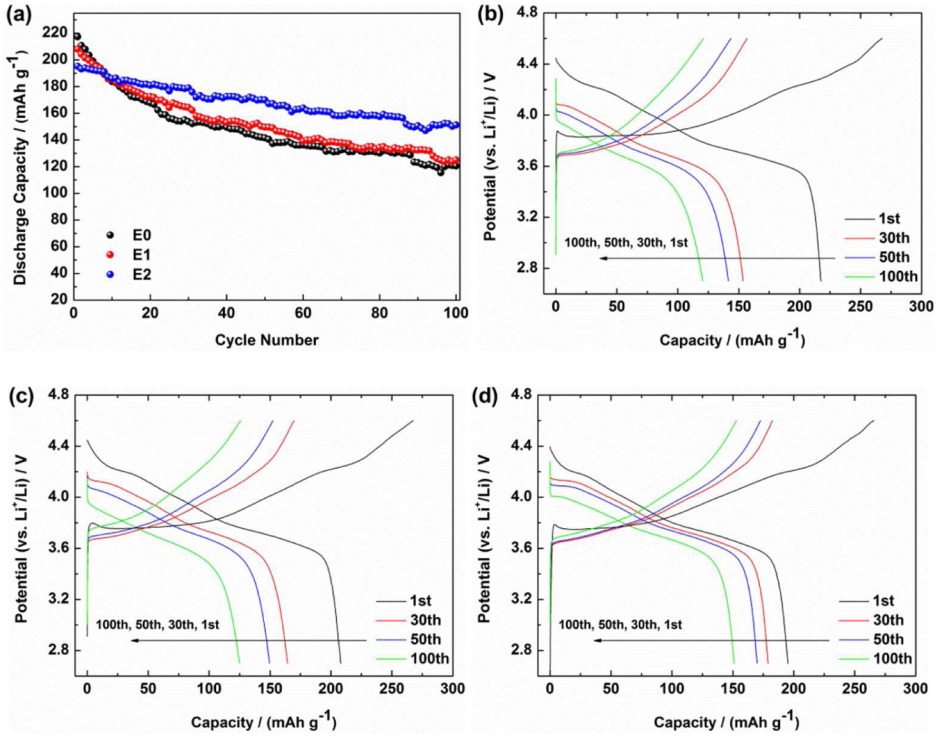

Figure 5. (a) Cycling performance of samples E0−E2 at 0.2 C and charge/discharge profiles of (b) E0, (c) E1, and (d) E2.

Table 3. Electrochemical Data of E0−E2 Cycling at 0.2 C

sample	initial charge capacity (mAh g^{-1})	initial discharge capacity (mAh g^{-1})	initial Coulombic efficiency (%)	100th discharge capacity (mAh g^{-1})	capacity retention after 100 cycles (%)
E0	267.6	217.4	81.2	120.6	55.5
E1	267.4	208.1	77.8	125	60.1
E2	266	195.3	73.4	151.2	77.3

151.2 mAh g^{-1} after 100 cycles (77.3% capacity retention). With the increase in the amount of the Li source, the larger primary particles produce a longer Li^+ diffusion pathway,[25,26] resulting in a lower capacity for the initial cycles and a lower initial Coulombic efficiency. However, the weaker Li^+/Ni^{2+} mixing gives rise to better cycling performance. It can be seen that E2 maintains the highest capacity after several cycles. The cycling performance of E3 is shown in Figure S3 of the Supporting Information, and the initial and 100th discharge capacities are only 113.8 and 75.1 mAh g^{-1}, respectively. The low capacity is due to the detrimental impact of $LiOH/Li_2CO_3$ impurities.

The working voltages of Ni-rich material will decrease during cycling for the polarization caused by Li^+/Ni^{2+} disorder.[27,28] Panels b−d of Figure 5 show the charge and discharge voltage profiles of E0−E2, respectively, between 2.7 and 4.6 V at 0.2 C after 1st, 30th, 50th, and 100th cycles. It should be noted that the average working voltages decrease more slowly with the increase in the amount of the Li source with an increase in cycle number. This indicates that the structural stability of E0−E2 is progressively enhanced by the decrease of Li^+/Ni^{2+} disorder.

The corresponding dQ/dV curves for the charge/discharge profiles of 1st, 30th, 50th and 100th cycles at 0.2 C are shown in Figure 6. Two main oxidation/reduction peaks for each curve could be observed. Peak I in the charging curves and peak I′ in the discharging curves are related to the oxidation/reduction of Ni^{2+}/Ni^{4+}, and peak II in the charging process and peak II′ in the discharging process are related to the oxidation/reduction of Co^{3+}/Co^{4+}. The differences between different cycles observed in the redox peaks are related to the Li^+/Ni^{2+} rearrangement. The potential of peaks I′ and II′ decreases during cycling for each sample. As the cycling proceeded, it was obviously noted that the working voltages generally decrease progressively more slowly for E0−E2. The dQ/dV curves account for the fact that the increase in Ni^{2+} content decreases the level of Li^+/Ni^{2+} disorder.

Rate capability is one of the most significant electrochemical characteristics of lithium rechargeable batteries required for EVs and renewable energy storage application. The rate performance of E0−E2 is characterized by discharging at different applied current densities (charging at 0.2 C) each for 100 cycles as shown in Figure 7. The corresponding 1st and 100th discharge capacities at 0.5, 1, 2, 5, and 10 C are listed in Table 4. Similar to that of 0.2 C, although the initial discharge capacity decreases progressively for E0−E2, the cycling stability is improved at various rates. The rate performance of sample E3 is exhibited in Figure S4 of the Supporting Information. We can see that the discharge capacity is exremely low at different rates, revealing the poor rate performance of E3 caused by $LiOH/Li_2CO_3$ impurities.

EIS spectra of samples E0−E2 has been measured before cycling and after 100 cycles charged to 4.2 V (as shown in Figure 8). All the plots consist of two semicircles in the high-frequency region and a slope in the low-frequency region. As a result, the intercept of the semicircle at the highest frequency with the real axis (Z') refers to uncompensated ohmic resistance (R_s), the semicircle at the highest frequency is assigned to the diffusion of Li^+ through the SEI film (R_{SEI}), the semicircle in the high- to medium-frequency region is related to the surface charge transfer process (R_{ct}), and the slope in the low-frequency region corresponds to a Warburg diffusion

DOI: 10.1021/acsami.5b00645
ACS Appl. Mater. Interfaces 2015, 7, 7702−7708

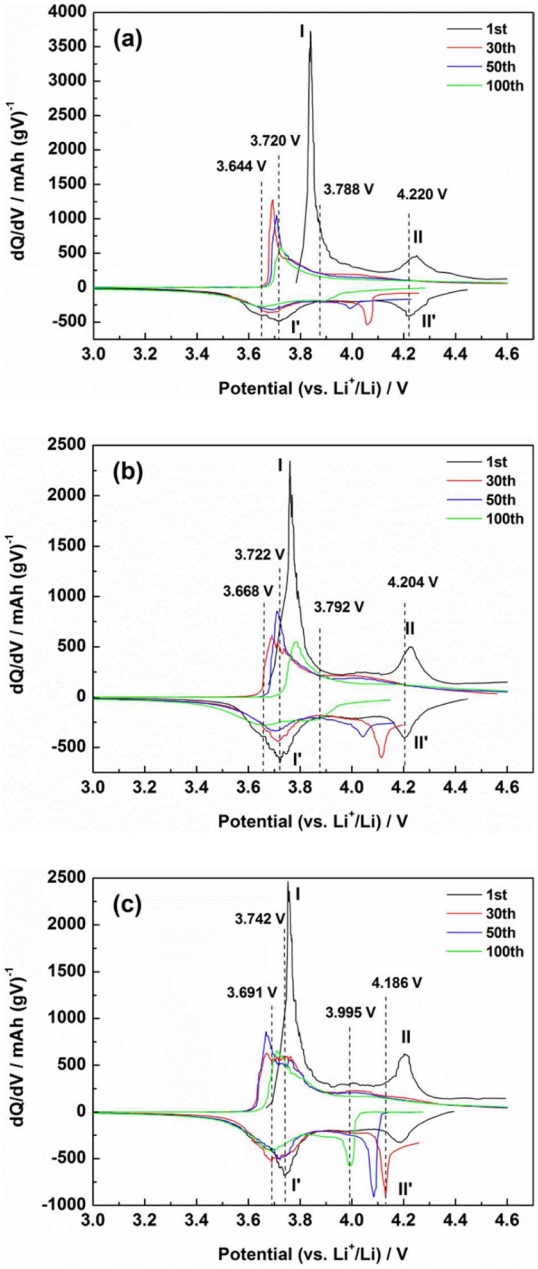

Figure 6. Differential capacity vs voltage curves of different numbers of cycles at 0.2 C for samples (a) E0, (b) E1, and (c) E2.

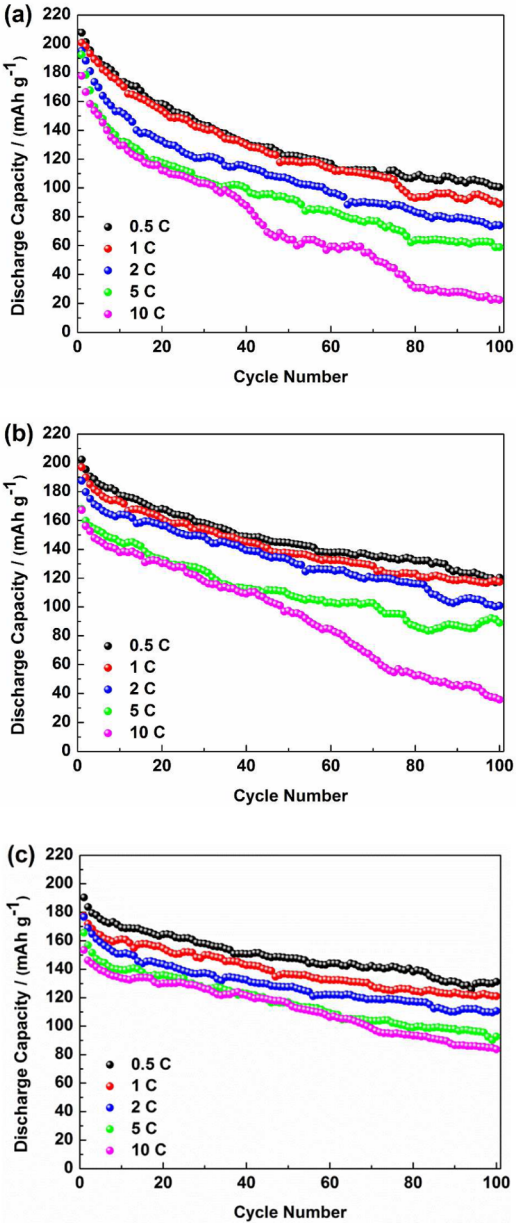

Figure 7. Rate performance of samples (a) E0, (b) E1, and (c) E2: cycling under rates of 0.5, 1, 2, 5, and 10 C each for 100 cycles.

process.[29−31] The obtained EIS spectra are simulated using the equivalent circuit exhibited at the bottom of Figure 8. The fitting results of R_s, R_{SEI}, and R_{ct} for samples E0−E2 are shown in Table 5. It can be seen that both samples show negligible ohmic resistance of 2.5−7.5 Ω. After 100 cycles, R_{ct} is so greatly increased for all the samples that R_{SEI} can be relatively neglected. The R_{ct} before cycling is progressively increased for samples E0−E2, but it presents an inverse result after 100 cycles. This suggests that Li^+/Ni^{2+} disorder is suppressed with the increase in the amount of the Li source, which contributes to the better cycling ability and rate capability.

The XRD patterns of samples E0−E2 after 100 cycles are exhibited in Figure 9. All the peaks become broader after cycling compared with those of the pristine samples, indicating that the structural damage occurs during cycling. The indistinct splitting of (006)/(102) and (018)/(110) peaks explains that the layered structure is damaged to some extent, which is caused by the irreversible phase transition, and the level of Li^+/Ni^{2+} disorder is increased,[6] which leads to the decrease in capacity during cycling. The ionic radius of Ni^{2+} (0.069 nm) is larger than that of Ni^{3+} (0.056 nm), and a larger Ni^{2+}/Ni^{3+} ratio can stabilize the structure, decreasing the level of Li^+/Ni^{2+} disorder and structural change during cycling. The I_{003}/I_{104} ratios of E0−E2 are 1.257, 1.350, and 2.007, respectively. This further certifies the level of Li^+/Ni^{2+} disorder decreases with an increase in Ni^{2+} content.

4. CONCLUSION

In our work, Ni-rich layered $LiNi_{0.8}Co_{0.1}Mn_{0.1}O_2$ with different levels of Ni^{2+} has been successfully prepared by sintering the $Ni_{0.8}Co_{0.1}Mn_{0.1}(OH)_2$ spheres with different amounts of the Li source. The cycling performance and rate capability are enhanced with an increase in Ni^{2+} content. The level of $Li^+/$

DOI: 10.1021/acsami.5b00645
ACS Appl. Mater. Interfaces 2015, 7, 7702−7708

Table 4. Electrochemical Data of E0−E2 Cycling at 0.5, 1, 2, 5, and 10 C

	0.5 C		1 C		2 C		5 C		10 C	
sample	1st (mAh g^{-1})	100th (mAh g^{-1})	1st (mAh g^{-1})	100th (mAh g^{-1})	1st (mAh g^{-1})	100th (mAh g^{-1})	1st (mAh g^{-1})	100th (mAh g^{-1})	1st (mAh g^{-1})	100th (mAh g^{-1})
E0	207.6	100.6	200.7	88.9	195.2	74.1	192.4	58.9	177.8	22.5
E1	202.2	120.3	196.9	117.3	187.5	100.9	168.0	88.9	167.2	35.8
E2	190.4	131.2	177.4	121.0	176.7	110.7	165.7	92.8	153.4	83.8

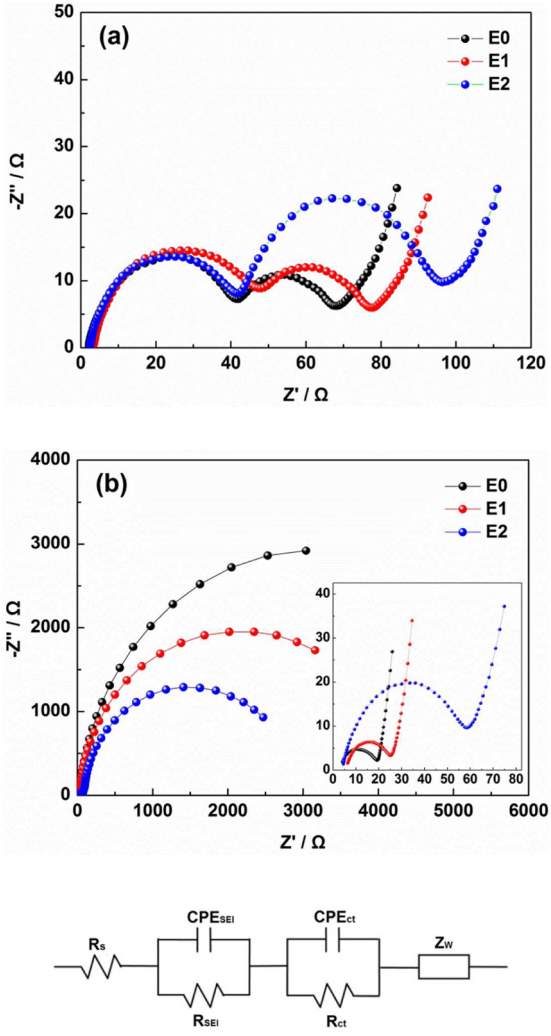

Figure 8. Nyquist plots of samples E0−E2 (a) before cycling and (b) after 100 cycles charged to 4.2 V.

Ni^{2+} disorder decreases with an increase in Ni^{2+} content, improving the electrochemical properties and structural stability during cycling. Thus, we conclude that an appropriate excess amount of Li reducing the Ni^{3+} to Ni^{2+} is an effective method for overcoming the existing problems of Li^{+}/Ni^{2+} disorder in Ni-rich cathode materials for high-power applications.

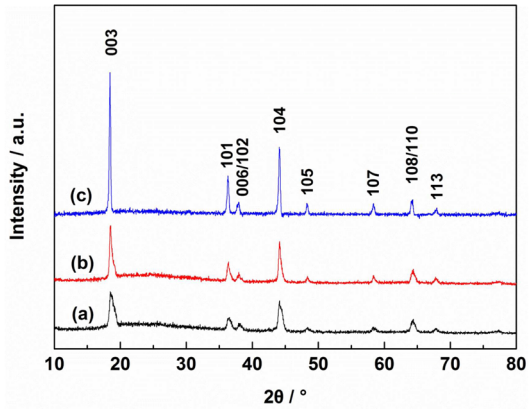

Figure 9. XRD patterns of samples (a) E0, (b) E1, and (c) E2 after 100 cycles.

■ ASSOCIATED CONTENT

Supporting Information

SEM images and XRD patterns of sample E3 (Figure S1), XPS spectra of Mn 2p and Co 2p for samples E0−E2 (Figure S2), cycling performance of sample E3 at 0.2 C charge/discharge (Figure S3), rate performance of sample E3 determined via cycling under rates of 0.5, 1, 2, 5, and 10 C each for 100 cycles (Figure S4). This material is available free of charge via the Internet at http://pubs.acs.org.

■ AUTHOR INFORMATION

Corresponding Author

*Telephone: +86-10-6891-8099. Fax: +86-10-6891-8200. E-mail: suyuefeng@bit.edu.cn.

Notes

The authors declare no competing financial interest.

■ ACKNOWLEDGMENTS

This work was funded by the Chinese National 973 Program (2015CB251100), the National Natural Science Foundation of China (51472032 and 51202083), the Program for New Century Excellent Talents in University (NCET-13-0044), the Special Fund of Beijing Co-construction Project and BIT Scientific and Technological Innovation Project (2013CX01003), and the Beijing Science and Technology Committee (Z131100003413001).

Table 5. Impedence Data of E0−E2 Charged to 4.2 V before Cycling and after 100 Cycles

	E0			E1			E2		
cycling	R_s (Ω)	R_{SEI} (Ω)	R_{ct} (Ω)	R_s (Ω)	R_{SEI} (Ω)	R_{ct} (Ω)	R_s (Ω)	R_{SEI} (Ω)	R_{ct} (Ω)
before	2.784	26.19	32.26	4.258	31.03	34.65	3.201	34.54	48.85
after	4.511	11.95	5294	7.051	15.21	3609	5.186	43.38	2064

DOI: 10.1021/acsami.5b00645
ACS Appl. Mater. Interfaces 2015, 7, 7702−7708

REFERENCES

(1) Armand, M.; Tarascon, J. M. Building Better Batteries. *Nature* **2008**, *451*, 652−657.

(2) Dunn, B.; Kamath, H.; Tarascon, J.-M. Electrical Energy Storage for the Grid: A Battery of Choices. *Science* **2011**, *334*, 928−935.

(3) Manthiram, A.; Vadivel Murugan, A.; Sarkar, A.; Muraliganth, T. Nanostructured Electrode Materials for Electrochemical Energy Storage and Conversion. *Energy Environ. Sci.* **2008**, *1*, 621−638.

(4) Goodenough, J. B.; Kim, Y. Challenges for Rechargeable Li Batteries. *Chem. Mater.* **2010**, *22*, 587−603.

(5) Choi, N. S.; Chen, Z.; Freunberger, S. A.; Ji, X.; Sun, Y. K.; Amine, K.; Yushin, G.; Nazar, L. F.; Cho, J.; Bruce, P. G. Challenges Facing Lithium Batteries and Electrical Double-Layer Capacitors. *Angew. Chem.* **2012**, *51*, 9994−10024.

(6) Kim, Y. Lithium Nickel Cobalt Manganese Oxide Synthesized Using Alkali Chloride Flux: Morphology and Performance as a Cathode Material for Lithium Ion Batteries. *ACS Appl. Mater. Interfaces* **2012**, *4*, 2329−2333.

(7) Cho, Y.; Lee, S.; Lee, Y.; Hong, T.; Cho, J. Spinel-Layered Core-Shell Cathode Materials for Li-Ion Batteries. *Adv. Energy Mater.* **2011**, *1*, 821−828.

(8) Sun, Y.-K.; Kim, D.-H.; Yoon, C. S.; Myung, S.-T.; Prakash, J.; Amine, K. A Novel Cathode Material with a Concentration-Gradient for High-Energy and Safe Lithium-Ion Batteries. *Adv. Funct. Mater.* **2010**, *20*, 485−491.

(9) Cho, Y.; Oh, P.; Cho, J. A New Type of Protective Surface Layer for High-Capacity Ni-Based Cathode Materials: Nanoscaled Surface Pillaring Layer. *Nano Lett.* **2013**, *13*, 1145−1152.

(10) Kim, K. J.; Jo, Y. N.; Lee, W. J.; Subburaj, T.; Prasanna, K.; Lee, C. W. Effects of Inorganic Salts on the Morphological, Structural, and Electrochemical Properties of Prepared Nickel-Rich Li-$[Ni_{0.6}Co_{0.2}Mn_{0.2}]O_2$. *J. Power Sources* **2014**, *268*, 349−355.

(11) Hwang, S.; Kim, S. M.; Bak, S. M.; Cho, B. W.; Chung, K. Y.; Lee, J. Y.; Chang, W.; Stach, E. A. Investigating Local Degradation and Thermal Stability of Charged Nickel-Based Bathode Materials Through Real-Time Electron Microscopy. *ACS Appl. Mater. Interfaces* **2014**, *6*, 15140−15147.

(12) Yu, H.; Qian, Y.; Otani, M.; Tang, D.; Guo, S.; Zhu, Y.; Zhou, H. Study of The Lithium/Nickel Ions Exchange in the Layered $LiNi_{0.42}Mn_{0.42}Co_{0.16}O_2$ Cathode Material for Lithium Ion Batteries: Experimental and First-Principles Calculations. *Energy Environ. Sci.* **2014**, *7*, 1068−1078.

(13) Sun, Y. K.; Lee, D. J.; Lee, Y. J.; Chen, Z.; Myung, S. T. Cobalt-Free Nickel Rich Layered Oxide Cathodes for Lithium-Ion Batteries. *ACS Appl. Mater. Interfaces* **2013**, *5*, 11434−11440.

(14) Dolotko, O.; Senyshyn, A.; Mühlbauer, M. J.; Nikolowski, K.; Ehrenberg, H. Understanding Structural Changes in NMC Li-Ion Cells by in Situ Neutron Diffraction. *J. Power Sources* **2014**, *255*, 197−203.

(15) Wu, F.; Tian, J.; Su, Y.; Guan, Y.; Jin, Y.; Wang, Z.; He, T.; Bao, L.; Chen, S. Lithium-Active Molybdenum Trioxide Coated $LiNi_{0.5}Co_{0.2}Mn_{0.3}O_2$ Cathode Material with Enhanced Electrochemical Properties for Lithium-Ion Batteries. *J. Power Sources* **2014**, *269*, 747−754.

(16) Meng, X.; Yang, X. Q.; Sun, X. Emerging Applications of Atomic Layer Deposition for Lithium-Ion Battery Studies. *Adv. Mater. (Weinheim, Ger.)* **2012**, *24*, 3589−3615.

(17) Xia, S.; Zhang, Y.; Dong, P.; Zhang, Y. Improve Electrochemical Performance of CeO_2 Surface Modification $LiNi_{0.80}Co_{0.15}Al_{0.05}O_2$ Cathode Material. *Eur. Phys. J.: Appl. Phys.* **2014**, *66*, 30403.

(18) Sun, Y.-K.; Myung, S.-T.; Kim, M.-H.; Prakash, J.; Amine, K. Synthesis and Characterization of Li-$[(Ni_{0.8}Co_{0.1}Mn_{0.1})_{0.8}(Ni_{0.5}Mn_{0.5})_{0.2}]O_2$ with the Microscale Core-Shell Structure as the Positive Electrode Material for Lithium Batteries. *J. Am. Chem. Soc.* **2005**, *127*, 13411−13418.

(19) Du, K.; Hua, C.; Tan, C.; Peng, Z.; Cao, Y.; Hu, G. A High-Powered Concentration-Gradient $Li(Ni_{0.85}Co_{0.12}Mn_{0.03})O_2$ Cathode Material for Lithium Ion Batteries. *J. Power Sources* **2014**, *263*, 203−208.

(20) Sun, Y.-K.; Myung, S.-T.; Park, B.-C.; Amine, K. Synthesis of Spherical Nano- to Microscale Core-Shell Particles Li-$[(Ni_{0.8}Co_{0.1}Mn_{0.1})_{1-x}(Ni_{0.5}Mn_{0.5})_x]O_2$ and Their Applications to Lithium Batteries. *Chem. Mater.* **2006**, *18*, 5159−5163.

(21) Li, D.-C.; Muta, T.; Zhang, L.-Q.; Yoshio, M.; Noguchi, H. Effect of Synthesis Method on the Electrochemical Performance of $LiNi_{1/3}Mn_{1/3}Co_{1/3}O_2$. *J. Power Sources* **2004**, *132*, 150−155.

(22) Li, D.; Sasaki, Y.; Kobayakawa, K.; Sato, Y. Morphological, Structural, and Electrochemical Characteristics of $LiNi_{0.5}Mn_{0.4}M_{0.1}O_2$ (M = Li, Mg, Co, Al). *J. Power Sources* **2006**, *157*, 488−493.

(23) Kim, J.; Hong, Y. S.; Ryu, K. S.; Kim, M. G.; Cho, J. Washing Effect of a $LiNi_{0.83}Co_{0.15}Al_{0.02}O_2$ Cathode in Water. *Electrochem. Solid-State Lett.* **2006**, *9*, A19−A23.

(24) Liu, H. S.; Yang, Y.; Zhang, J. J. Investigation and Improvement on the Storage Property of $LiNi_{0.8}Co_{0.2}O_2$ as a Cathode Material for Lithium-Ion Batteries. *J. Power Sources* **2006**, *162*, 644−650.

(25) Zhu, J.; Fiore, J.; Li, D.; Kinsinger, N. M.; Wang, Q.; DiMasi, E.; Guo, J.; Kisailus, D. Solvothermal Synthesis, Development, and Performance of $LiFePO_4$ Nanostructures. *Cryst. Growth Des.* **2013**, *13*, 4659−4666.

(26) Liu, J.; Chen, H.; Xie, J.; Sun, Z.; Wu, N.; Wu, B. Electrochemical Performance Studies of Li-Rich Cathode Materials with Different Primary Particle Sizes. *J. Power Sources* **2014**, *251*, 208−214.

(27) Jorn, R.; Kumar, R.; Abraham, D. P.; Voth, G. A. Atomistic Modeling of the Electrode−Electrolyte Interface in Li-Ion Energy Storage Systems: Electrolyte Structuring. *J. Phys. Chem. C* **2013**, *117*, 3747−3761.

(28) Norberg, N. S.; Lux, S. F.; Kostecki, R. Interfacial side-reactions at a $LiNi_{0.5}Mn_{1.5}O_4$ electrode in organic carbonate-based electrolytes. *Electrochem. Commun.* **2013**, *34*, 29−32.

(29) Li, P.; Liu, H.; Lu, B.; Wei, Y. Formation Mechanism of 1D ZnO Nanowhiskers in Aqueous Solution. *J. Phys. Chem. C* **2010**, *114*, 21132−21137.

(30) Liu, J.; Manthiram, A. Functional Surface Modifications of a High Capacity Layered $Li\ Li_{0.2}Mn_{0.54}Ni_{0.13}Co_{0.13}O_2$ Cathode. *J. Mater. Chem.* **2010**, *20*, 3961−3967.

(31) Qiu, X.-Y.; Zhuang, Q.-C.; Zhang, Q.-Q.; Cao, R.; Qiang, Y.-H.; Ying, P.-Z.; Sun, S.-G. Reprint of "Investigation of layered $LiNi_{1/3}Co_{1/3}Mn_{1/3}O_2$ Cathode of Lithium Ion Battery by Electrochemical Impedance Spectroscopy". *J. Electroanal. Chem.* **2013**, *688*, 393−402.

DOI: 10.1021/acsami.5b00645
ACS Appl. Mater. Interfaces 2015, 7, 7702−7708